Gyrokinetic Simulations of Tokamak Microturbulence

W. Dorland, B. N. Rogers, F. Jenko (1), M. Kotschenreuther (2), G. W. Hammett (3), D. Mikkelsen (3), D. W. Ross (4), M. A. Beer (3), P. B. Snyder (5), R. Bravenec (4), M. Greenwald (6), D. Ernst (3), R. Budny (3)

University of Maryland, College Park, Maryland, 20742, USA
(1) Max-Planck-Institut für Plasmaphysik, EURATOM, 85748 Garching, Germany
(2) Institute for Fusion Studies, University of Texas, Austin, Texas, 78712 (3) Princeton Plasma Physics Laboratory, Princeton, NJ, 08543 (4) Fusion Research Center, University of Texas, Austin, Texas, 78712 (5) General Atomics, La Jolla, CA (6) Plasma Science and Fusion Center, MIT, Cambridge, MA, 02139

Abstract

Gyrokinetic simulations of ITG ($k_\perp \rho_i \lesssim 1$) and ETG ($k_\perp \rho_i \gg 1$) turbulence are presented. Comparisons of toroidal turbulence in these two limits provide insights into the dynamics of streamers and zonal flows. We address the generation of zonal flows by secondary instabilities and the regulation of zonal flows by collisionless tertiary instabilities. We present the first toroidal electromagnetic gyrokinetic simulations of small scale turbulence, and gyrofluid models which explain two important gyrokinetic results: (1) Near marginal stability of the linear ITG mode, the turbulence can generate zonal flows that are sufficiently weak to remain stable but sufficiently strong to suppress the linear ITG mode. This stable region corresponds to the parameter regime of the nonlinear Dimits shift. (2) "Long" wavelength ($k_\perp \rho_i \gg 1 > k_\perp \rho_e$) ETG turbulence drives experimentally relevant thermal transport, because the secondary modes that produce saturation become weak. Finally, preliminary comparisons of simulations with experimental data are described.

1 Introduction

Numerical simulations of ion-temperature-gradient (ITG) driven modes in magnetically confined fusion plasmas indicate that poloidal $\mathbf{E} \times \mathbf{B}$ flows, spontaneously generated by the nonlinear dynamics, play a central role in regulating the saturation level of the turbulence and the resulting cross-field heat transport[1]. This is strikingly evident in simulations near marginally stable conditions, in which the sheared flows generated by the system virtually suppress all transport, and lead to an effective nonlinear upshift of the critical ITG mode instability gradient [2] (the "Dimits" shift). In the context of the electrostatic ITG system, we address [3] three fundamental questions regarding these sheared poloidal (or "zonal") flows. First, what is the mechanism by which these flows are generated? Second, under what conditions are these flows stable? And third, are these flows experimentally relevant? In the course of answering these questions, we shall obtain a clearer understanding of the Dimits shift, and some insight into the impact it is likely to have on ITG-based transport models [4].

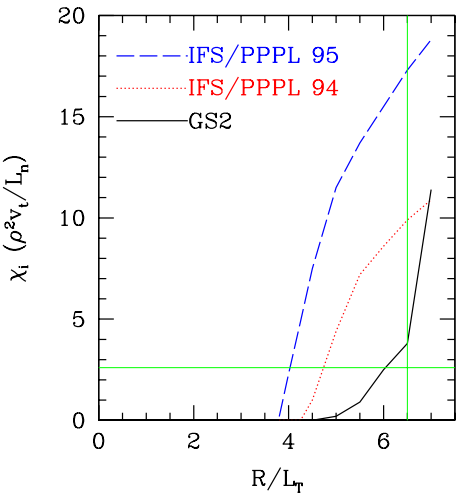

Figure 1: *Gyrokinetic simulation (*GS2*) explains disagreement between IFS/PPPL models and this C-Mod data from the ITER profile database; experimental data shown by horizontal and vertical lines (#960116027,* $\rho = 0.5, t = 0.90, R/L_{Tcrit} = 4.5$.

The equations which describe electrostatic microinstabilities driven by electron temperature gradients [5] (ETG) and by ion temperature gradients [6] (ITG) are very similar. In fact, the

linear instabilities are exactly the same, except that the species labels for length and time scales are exchanged. The length scales are the Larmor radius of the non-adiabatic species, *i.e.*, ρ_e and ρ_i respectively. The time scales for the two modes are L_{Te}/v_{te} and L_{Ti}/v_{ti}, where L_{Ts} and v_{ts} are the equilibrium temperature gradient scale length and thermal velocity for species s.

In a typical fusion plasma, $\rho_i \sim 60\rho_e$ and $v_{te} \sim 60 v_{ti}$, so that electron scale turbulence is characterized by shorter wavelengths and higher frequencies. Simple mixing length arguments suggest $\chi_s \sim \rho_s^2 v_{ts}/L_{Ts} \equiv \chi_{s0}$, so that $\chi_i \sim 60\chi_e$. For ETG transport to be experimentally important, the normalized χ/χ_{e0} from ETG simulations should be much larger than the normalized χ/χ_{i0} from ITG simulations. Nonlinear, electromagnetic, toroidal, gyrokinetic (and gyrofluid) simulations of ETG turbulence find this behavior [see Fig. (2)].

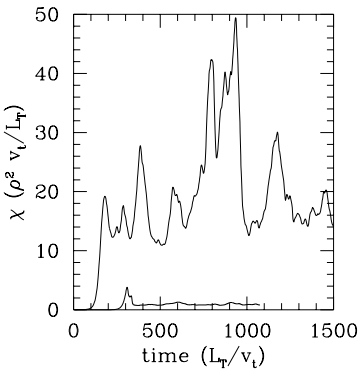

Figure 2: $\chi_e^{\rm ETG}$ *(upper) and* $\chi_i^{\rm ITG}$ *(lower) for similar (Cyclone) parameters, except* $\alpha = 0.45$ *in EM ETG case. [10, 11]*

It is often the case that experimentally inferred electron and ion thermal diffusivities are comparable because significant electron transport is driven by ion-scale turbulence, mostly as a result of the non-adiabatic response of electrons which are trapped in low magnetic field regions. This is the origin of electron thermal transport in the IFS/PPPL [4] model, for example. However, there are experimental cases [7, 8] in which distinctly anomalous electron thermal transport is observed without accompanying anomalous ion thermal transport or ion-scale fluctuations. Below, we argue that ETG turbulence is a reasonable candidate for explaining experimental observations such as these. We also provide a simple model that explains why ETG transport is larger than one might expect from linear theory.

The models we develop to describe our ETG and ITG simulations are in the spirit of Ref. [9].

2 Zonal Flows and ITG Turbulence

Insight into the generation of zonal flows by ITG modes can be obtained by an examination of a nonlinear gyrokinetic simulation just prior to the onset of turbulent saturation. [3] During this phase, a burst of zonal flow growth is observed that is qualitatively similar to (but more extreme than) bursts that are observed throughout the turbulent phase. Starting the simulation from small amplitude random perturbations, a dominant (primary) linear ITG mode emerges in the linear phase. Fig. (3) shows the growth rate γ_l (dotted line) of this linear mode as a function of time, from the linear phase through the initial saturation, with the normalizations $\phi = e\phi_{phys}R/(\rho_{se}T_{e0})$, $\rho_{se} = c_{se}/\Omega_{ci}$, $c_{se} = \sqrt{T_{e0}/m_i}$, $t = t_{phys}c_{se}/R$, $\gamma_l = \gamma_{l,phys}R/c_{se}$. The parameters used in the simulation are $R/L_T = 6.9$, $R/L_n = 2.2$, $T_i/T_e = 1$, $\hat{s} = 0.8$, and $r/R = 0.167$. For these parameters the dominant linear mode produces the usual pattern of radial streamers at a well defined poloidal wavenumber: $k_y = 0.3 = (0.3/\rho_{se})$ and $k_x = 0$, where x, y are flux tube radial and poloidal coordinates[12].

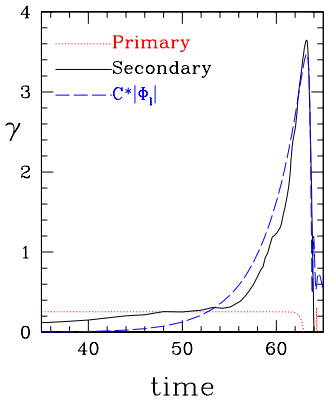

Figure 3: *Growth rates.*

The solid curve in Fig. (3) shows the growth rate of the fastest growing zonal flow mode ($k_x \simeq 0.4$) in the simulation. In general, the growth rates of the zonal flow modes exhibit a k_x spectrum unrelated to that of the primary ITG instability. A snapshot (at $t = 62.3$) of the instantaneous

growth rates of the zonal modes vs. k_x is shown in Fig.(4). For comparison, the linear growth rates *vs.* k_x for $k_y = 0.3$ are also shown. The secondary growth rates increase with the amplitude of the primary mode, $\gamma \propto \phi_l \propto e^{\gamma_l t}$. Just before nonlinear saturation, $\gamma \gg \gamma_l$. This can be seen from the solid line in Fig. (3). For comparison, the dashed line in Fig. (3) represents the curve $\gamma_\phi = C k_y |\phi_l|$, where $C = 0.2$ has been chosen to yield $\gamma_\phi = \gamma$ at the time of Fig. (4), $t = 62.3$. We obtain $C = 0.3$ below from a simple model.

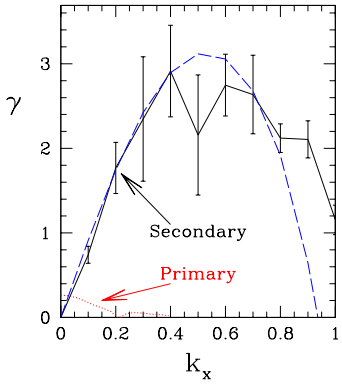

Figure 4: *Observed secondary mode growth rates vs. k_x.*

Motivated by these observations, we focus on the behavior just before saturation, when the secondary modes have small amplitudes compared to the primary, but have growth rates $\gamma \gg \gamma_l$. It is during this phase, in which the finite-k_x modes grow roughly as the exponential of an exponential, that the bulk of the zonal flow is generated. In this regime the secondary modes can be analyzed in the context of a linear stability analysis, treating the linear ITG mode eigenfunction as a static, quasi-equilibrium background. The radial streams associated with this ITG mode background state then drive a KH-like instability with $\gamma \propto |\phi_l|$, and a k_x spectrum that is in good agreement with the simulations. These KH-like eigenmodes necessarily possess a zonal flow component, and provide a natural nonlinear mechanism through which zonal flows are created throughout the simulation.

Our analysis is based on the electrostatic gyrofluid model with adiabatic electrons [13]. At the time of interest, at which the growth rates of secondary modes exceed $k_\| v_{th,i}$ (taking $k_\| \sim 1/(qR)$, for example), n and $T_\perp$ decouple from the other moments. The model is further simplified by neglecting the usual linear contributions from the equilibrium magnetic curvature, shear, and background gradients, which are weak compared to the nonlinear driving terms. The resulting equations, dropping terms of order $(k_\perp \rho_i)^4$ compared to unity, are

$$\frac{dn}{dt} + \frac{1}{2}\left[\tau \nabla_\perp^2 \psi, T_\perp\right] = 0\,, \qquad \frac{dT_\perp}{dt} = 0, \tag{1}$$

where $d/dt = \partial/\partial t + [\psi, \cdot]$, ψ is the guiding center electrostatic potential, and $n = \psi - \langle\psi\rangle - \nabla_\perp^2[(1+\tau)\psi - \tau\langle\psi\rangle + \tau T_\perp/2]$. Length scales are normalized to ρ_{se}, $\tau = T_{i0}/T_{e0}$, $n = n_{phys}R/(\rho_{se} n_0)$, $T_\perp = T_{\perp,phys}R/(\rho_{se} T_{i0})$, $\psi = e\psi_{phys}R/(\rho_{se} T_{e0})$. Angle brackets denote a flux surface average, and reduce in the high amplitude (2D) limit to an average over y. We next take $\psi = \psi_l(y) + \tilde{\psi}(y)\exp(\gamma t + i k_x x)$, $T_\perp = T_l(y) + \tilde{T}_\perp(y)\exp(\gamma t + i k_x x)$, where $\psi_l(y)$, $T_l(y)$ represent a periodic configuration of radial streams similar to that produced by the linear ITG mode, *e.g.*, $\psi_l(y) = \psi'_{l0}\sin(k_l y)/k_l$, $T_l(y) = T'_{l0}\sin(k_l y + \delta)/k_l$, for various constants ψ'_{l0}, T'_{l0}, k_l, δ. Linearizing in $\tilde{\psi}$,$\tilde{T}_\perp$, and noting $\langle\psi_l\rangle = 0$, one finds

$$-(1+\tau k_x^2)\bar{\gamma}\langle\tilde{\psi}\rangle + \left[\gamma + k_x^2\Gamma\right]\tilde{\psi} = \partial_y\left[\Gamma\bar{\gamma}\partial_y(\tilde{\psi}/\bar{\gamma})\right] \tag{2}$$

with $\Gamma = \tau\gamma + \bar{\gamma}_T$, $\bar{\gamma} = \gamma - i k_x \psi'_l(y)$, $\bar{\gamma}_T = \gamma - i k_x[(1+\tau)\psi'_l(y) + \tau T'_l(y)]$. In general, this eigenvalue problem must be solved numerically. In the typical case $k_l^2 \ll 1$ relevant to the simulations, however, an analytic solution for ψ may be obtained as a power-series in k_l^2 by treating the right hand side as small, $O(k_l^2)$. To lowest order, the solution is

$$\tilde{\psi} = \frac{\bar{\gamma}\langle\tilde{\psi}\rangle}{\gamma + f(k_x)\bar{\gamma}_T}\,, \qquad f(k_x) = \frac{k_x^2}{1+\tau k_x^2}\,. \tag{3}$$

The (lowest order) dispersion relation follows by integrating this equation over y. Using the identity $\langle\bar{\gamma}/\gamma\rangle = 1$ valid for the periodic case, it may be written as

$$\langle\frac{\bar{\gamma}\bar{\gamma}_T}{\gamma + f(k_x)\bar{\gamma}_T}\rangle = 0 \tag{4}$$

In the limit $k_x^2 \ll 1$, this reduces to $\langle \bar{\gamma}\bar{\gamma}_T \rangle \simeq 0$. In the usual ITG case that $\psi_l(y)$ ($\simeq \phi_l(y)$ for $k_l \ll 1$) and $T_l(y)$ are $\pi/2$ out of phase, $T_l(y)$ makes no contribution, and one obtains $\gamma = [(1+\tau)/2]^{1/2}|k_x\phi'_{l0}|$ for $\phi_l(y) = \phi'_{l0}\sin(k_l y)/k_l$. This growth rate, $\gamma \sim k_x\phi'_{l0} = k_x V$, is similar to that of the well-known KH instability in the limit $k_x \ll k_l$. For the KH mode, the maximum growth rate $\gamma_{max} \sim k_l V$ is reached for $k_x \sim k_l$, and stability is obtained for $k_x > k_l$. In the present case, on the other hand, the expansion of Eq. (4) remains valid until $k_x \sim 1 \gg k_l$, leading to the much larger growth rate $\gamma_{max} \sim V$ at $k_x \sim 1$ (ie, $k_x\rho_{se} \sim 1$). For example, for $\tau = 0$, one finds $\gamma = k_x\phi'_{l0}[(1-k_x^2)/(2-k_x^4)]^{1/2}$.

For $k_x \sim 1$, the assumption $\tau k_\perp^2$ $[= (k_\perp\rho_i)^2] \ll 1$ made in deriving Eq. (1) requires $\tau \ll 1$. However, for $k_l \ll 1$, one can easily retain all orders in $k_x\rho_i$. The result, to lowest order in k_l^2, is the same as Eqns. (3–4), with the replacements $f(k_x) = (1-\Gamma_0)/\tau$, $\bar{\gamma}_T = \gamma - ik_x\{(1+\tau)\psi'_l(y) + [b\Gamma'_0/(1-\Gamma_0)]\tau T'_l(y)\}$ where $b = \tau k_x^2$, $\Gamma_0(b) = I_0(b)e^{-b}$, $I_0(b) = J_0(ib)$ is the modified Bessel function, and $\Gamma'_0 = d\Gamma_0/db$. Again considering sinusoidal perturbations with $T'_l = 0$, the dispersion relation gives

$$\gamma = \frac{[(1+\tau)/2]^{1/2}[1-(2+\tau)g]}{[1-(2+\tau)g+(1+\tau)g^2/2]^{1/2}}|k_x\phi'_{l0}|, \tag{5}$$

where $g = (1-\Gamma_0)/(\tau+1-\Gamma_0)$. Instability is obtained for $(2+\tau)g < 1$, which reduces for $\tau k_x^2 < 1$ to $(1+\tau)k_x^2$ $(= \rho_s^2 k_x^2) < 1$. This result for $\gamma_{NL} \equiv \gamma/|\phi'_{l0}|$ is plotted for $\tau = 1$ in Fig. (5) (solid line). The data points show the values obtained from a nonlinear gyrokinetic simulation of a 2D radial streamer in the small $k_l \ll 1$ limit, in the absence of curvature and magnetic shear. Applying this result to the parameters $k_l = 0.3$, $k_x = 0.4$ relevant to Fig. (3), we obtain $\gamma_\phi = Ck_l|\phi_l|$ with $C \simeq 0.3$.

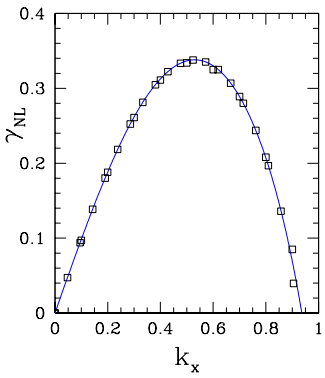

Figure 5: *Model and gyrokinetic secondary mode growth rates vs. k_x.*

In the simulations, the nonlinear evolution of the secondary modes just described produces zonal flows which ultimately break up the primary ITG streamers. The bulk of these zonal flows rapidly decay away on a timescale associated with transit-time damping. The dynamics of trapped particles in a toroidal geometry also leads, however, to an undamped residual component of the zonal flows [14], that near marginal linear stability is sufficient to nearly suppress further turbulence in the system. We now show this nonlinear, shear-flow-dominated state is itself subject to tertiary instabilities when the zonal flows exceed a critical threshold. Above this threshold, the tertiary modes are observed to grow to nonlinear amplitudes and damp the zonal flows. The threshold determines the upper boundary of the nonlinear Dimits upshift.

To illustrate this we examine the fate of small k_y perturbations in a pure zonal flow ($k_y = 0$, $k_x \neq 0$) equilibrium state. This state is obtained from a nonlinear gyrokinetic simulation just above marginal linear stability (*i.e.*, within the nonlinearly suppressed region), evolved out to late times when the system is dominated by the undamped, quasi-static zonal flows. The physics parameters used in this simulation are the same as before, except $R/L_T = 4.75$. The $\mathbf{E}\times\mathbf{B}$ shear in the simulation at late times arises predominantly from an undamped $k_x = 0.25$ component of ϕ, but other wavelength components of ϕ are also present, as are small $k_x \simeq 0.25$ components in $T_\perp$, $T_\parallel$, *etc.*

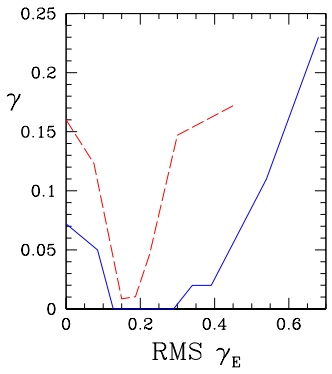

Figure 6: *Growth rates vs. RMS γ_E for $R/L_T = 4.75$ (dashed) and $R/L_T = 5.75$ (solid).*

We then artificially vary the average $\mathbf{E}\times\mathbf{B}$ shearing rate of this quasi-equilibrium relative to the rate actually observed in the simulation. Fig. (6) shows, as a function of the root-mean-square shearing rate γ_E, the measured growth rate of small $k_y \neq 0$ perturbations maximized over all k_y values. For $\gamma_E = 0$ (the usual linear case), the growth rate in the figure represents an ordinary ITG mode. This mode becomes progressively more stable as γ_E is increased, until absolute stability is attained at $\gamma_E = 0.13$. The actual (*i.e.*, non-scaled) γ_E value of the simulation falls in this stable range, consistent with its non-turbulent behavior at late times. As γ_E is increased further, however, a new instability sets in, with a growth rate that increases monotonically with the shear flow amplitude. This mode is localized to a spatial region in which the $\mathbf{E}\times\mathbf{B}$ shear is weak (an extremum of V_{Ey}), and propagates with the local $\mathbf{E}\times\mathbf{B}$ velocity at that location, $\omega \simeq k_y V_{Ey}$ with $k_y \simeq 0.7$. Before turning to a discussion of this new mode, we first make the important observation that this stability window does not exist for all parameters. Fig. (6) also shows the corresponding curve obtained with $R/L_T = 5.75$, in a region of parameter space in which nonlinear simulations display steady turbulence. At this value of R/L_T, the nonlinear suppression of turbulence is impossible because the zonal flows become unstable before the primary ITG mode can be shear flow stabilized.

To understand this, we consider a linear stability analysis of a shear flow dominated, x-dependent state like that found in the simulation. We focus on the limit in which the shear flow amplitudes associated with the quasi-equilibrium state become large. In that limit, as discussed earlier, the equations for n and $T_\perp$ (assuming fixed $k_\parallel$) decouple, and the contributions of the magnetic shear, curvature, and background gradients become weak. This is consistent with the simulations, which show the growth rate at large γ_E does not change if these effects are switched off. We therefore return to Eq. (1), and consider $\psi = \psi_0(x) + \tilde{\psi}(x)\exp(\gamma t + ik_y y)$, $T_\perp = T_0(x) + \tilde{T}_\perp(x)\exp(\gamma t + ik_y y)$, where $\psi_0(x)$, $T_0(x)$ now represent the static, x-dependent zonal flow background state. Upon linearizing in $\tilde{\psi}$,$\tilde{T}_\perp$, and noting that $\langle\psi\rangle = \psi_0$ (ie $\langle\tilde{\psi}\rangle = 0$), we obtain

$$\left[(1+(1+\tau)k_x^2)\bar{\gamma} + ik_y(k_y^2\tau T_0' - \tau\psi_0''')\right]\tilde{\psi} = \partial_x\left[(\tau\gamma + \bar{\gamma}_T)\bar{\gamma}\partial_x(\tilde{\psi}/\bar{\gamma})\right] \qquad (6)$$

with $\bar{\gamma} = \gamma + ik_y\psi_0'(x)$, $\bar{\gamma}_T = \gamma + ik_y[(1+\tau)\psi_0'(x) + \tau T_0'(x)]$. As noted earlier, the zonal flow state generated by the simulation on which Fig. (6) is based is dominated by a single $k_x \simeq 0.25$ mode in $\psi(x)$. A much smaller $k_x \simeq 0.25$ component in the ion temperature $T_0(x)$, π out of phase with that in $\psi_0(x)$, is also observed. In view of our earlier results, one might expect the small contribution from $T_0(x)$ in Eq. (6) could be neglected compared to that in ψ_0, but this is not the case. The simulations show the instability at large γ_E depends critically on the presence of both ψ_0 and T_0. This behavior is in agreement with our numerical study of Eq. (6), which predicts an instability very similar to that observed in the simulations. This instability is radially localized to the regions where the shearing rate $\propto \psi_0''$ vanishes, corresponding to extrema in both ψ_0' and T_0', and has a frequency $\omega \simeq -k_y\psi_0'$ ($\bar{\gamma} \simeq 0$). Upon expanding Eq. (6) about $x = x_0$ where $\psi_0'' = T_0'' = 0$, and defining $\lambda = (2\tau T_0'/\psi_0''')^{1/4}|_{x_0}$ (where $T_0'/\psi_0''' > 0$ by virtue of the phase relationship between T_0 and ψ_0), a simple scaling of the growth rate is obtained in the limit $k_x \ll 1$, in which λ ($\propto k_x^{-1/2}$) $\gg 1$. In this case, λ is found to represent the (normalized) radial scale of the mode, and one obtains a maximum growth rate $\gamma \simeq 0.55 k_y\sqrt{\tau T_0'\psi_0'''/2}$ for $k_y \simeq 1/\lambda$ that is in good agreement with the simulations.

At the more modest zonal flow amplitudes characteristic of the threshold region in Fig. (6), the behavior of the instability becomes substantially more complicated. One clear dependence of the stability threshold on the parameters, however, has been extracted from the simulations: increasing q in the runs of Fig. (6) from $q = 1.4$ to $q = 3$ eliminates the nonlinear upshift.

We now discuss preliminary experimental evidence which supports the relevance of the collisionless tertiary instability and the importance of the Dimits shift at low q. Detailed comparisons of data from DIII-D and C-Mod with general geometry gyrokinetic simulations including gyrokinetic electrons, impurities and collisions were undertaken. First results are shown in Fig. (1). This is a high collisionality, low ρ_*, 5T, ELMy H-mode C-Mod plasma [15] with 2.5 MW of ICRF heating for which the IFS/PPPL model (evaluated with $Z_{\rm eff} = 1.5$) is particularly pessimistic. At this radius, $q = 1.3$. Varying R/L_T around the experimental value, we find that the gyrokinetic transport is roughly as stiff as the IFS/PPPL models predict. However, the shift in R/L_{Tcrit} (from 4.5 to ~ 6, softened by the high collisionality [16]) clearly improves the agreement. The data suggest that lowering the collisionality would not change the temperature gradient much in this case, highlighting the potential importance of the collisionless mechanism described here.

3 Streamers and ETG Turbulence

ETG instabilities are characterized by $k_\theta \rho_e \sim 1$. Because $k_\perp \rho_i \gg 1$, the ion response to a perturbation is adiabatic: $n_i \sim \exp\{-Z|e|\Phi/T_i\}$. As a consequence, ETG turbulence drives no particle transport. ETG turbulence satisfies the nonlinear gyrokinetic[17] ordering. We use two independently developed parallel codes [10] to simulate the gyrokinetic Vlasov-Maxwell system, GENE and GS2. Reference parameters are the same as before, except $\alpha = 0.45$. For more details, see Refs. [10, 11].

The turbulent electric and magnetic fields induce radial thermal transport Q (defined in Ref. [10]). The thermal diffusivity is $\chi = Q/(-n^{(0)}\nabla T^{(0)})$, in units of χ_{s0}. As a check on the numerics, we have benchmarked GS2 and GENE. Also, GS2 reproduces [lower curve, Fig. (2), $\chi_i = 0.8\chi_{i0}$] the transport measured in GK PIC simulations [2] of electrostatic ITG turbulence.

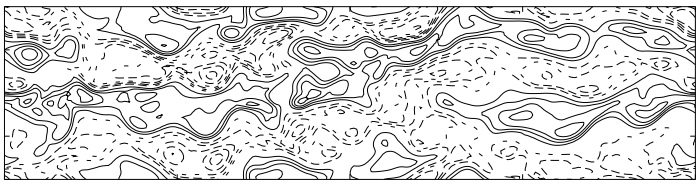

Figure 7: *Characteristic ϕ contours in the outboard x-y plane. This snapshot was taken at the end of the ETG run shown in Fig. 2. The figure is $256\rho_e \times 64\rho_e$.*

The turbulent thermal diffusivities *vs.* time shown in Fig. (2) are typical. We observe that large normalized ETG thermal transport is associated with high amplitude, radially elongated streamers at the outboard midplane in the turbulent steady state [Fig. (7)].

We now turn to a model which provides insight into the simulation results. Again, we consider primary, secondary and tertiary instabilities. We shall find that secondary modes in the ETG system are much weaker, and that unlike in the ITG system, the dynamics of secondary and tertiary modes in the ETG limit are similar.

First addressing the dynamics of secondary modes, we consider the electron version of Eqs. (1), again in the limit of a large amplitude primary. Only Poisson's equation differs; for ETG modes, $n = [\tau - (1+\tau)\nabla_\perp^2]\,\psi$. As for ITG modes, the relative phase of the temperature and density perturbations in the ETG eigenmode is such that the perpendicular temperature dynamics do not significantly affect the results, so we neglect $T_\perp$ here. Length scales are normalized to ρ_e, $\tau = Z_{\rm eff}T_{e0}/T_{i0}$, $n = n_{phys}L_{Te}/(\rho_e n_0)$, and $\psi = e\psi_{phys}L_{Te}/(\rho_e T_{e0})$.

Ignoring magnetic shear, we consider the linearization $\psi = \psi_p(y) + \tilde{\psi}(y)\exp(\gamma t + ik_x x)$, in which a crude model of the primary mode structure is given by $\psi_p(y) = \psi_{p0}\cos(k_p y)$. Here,

k_p represents the primary's poloidal wavenumber and ψ_{p0} determines its amplitude. One finds

$$\left[\left(\frac{\tau}{1+\tau}\right)\gamma + k_x^2\bar{\gamma}\right]\tilde{\psi} = \partial_y\left[\bar{\gamma}^2\partial_y(\tilde{\psi}/\bar{\gamma})\right] \tag{7}$$

with $\bar{\gamma} = \gamma - ik_x\psi_p'(y)$. The ETG secondary equation differs from conventional Kelvin-Helmholtz (KH) because of the first term on the left-hand side (the ion response). Balancing this term with the other terms in Eq. (7) leads to a maximum growth rate $\sim k_p^4\psi_{p0}$ for $k_x \sim k_p$. This growth rate is a factor of $(k_\perp\rho_e)^2$ smaller than conventional KH. Relative to ITG modes, whose secondary instability growth rates exceed conventional KH, secondary instabilities of ETG modes are quite weak, particularly for small $k_\perp\rho_e$. This weakening of the secondary instabilities at small $k_\perp\rho_e$ is the main reason that ETG turbulence saturates at high normalized levels for some parameters.

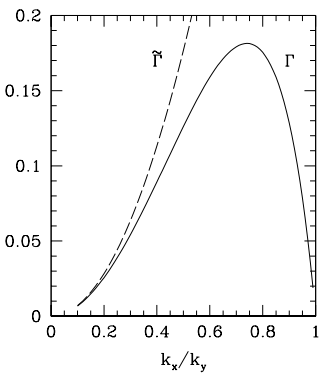

Figure 8: *Secondary instability growth rates for long wavelength ETG modes.*

A closed form solution of Eq. (7) exists in the limit $(k_x \ll k_p \ll 1)$, with eigenvalue $\gamma = \Gamma k_p^4(1+\tau^{-1})\psi_{p0}$, $\Gamma = (k_x/k_p)^2/\sqrt{2}$. For the less restrictive limit $k_p \ll 1$, Γ may be found numerically [Fig. (8)].

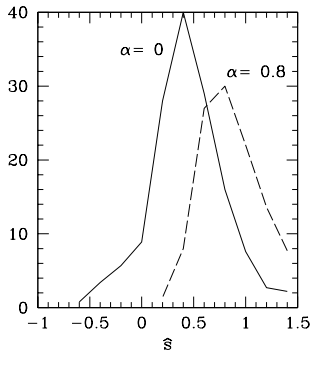

Figure 9: $\gamma/k_\perp^4$, *evaluated for the reference parameters, with varying* $\hat{s}$ *and* α.

For $\hat{s} \neq 0$, the primary modes twist with the field lines, causing the physical $k_\perp^2$ to exceed $k_x^2 + k_y^2$. This effect, which tends to enhance the growth rate of secondary modes, is reduced by the decrease in the primary mode amplitude along the field lines, and by higher order FLR terms not included here. The net result is typically a modest enhancement in γ and unstable k_x. The predictions of these models are in reasonable agreement with the secondary instability growth rates observed in nonlinear gyrokinetic ETG simulations. [11]

Balancing the primary and secondary mode growth rates produces a scaling for the normalized saturation level of the primary modes, $\phi_{\rm sat} \sim \gamma_l/k_\perp^4$. For comparison with nonlinear simulation results, we maximize this expression over k_x and k_y using the growth rate of the toroidal ETG mode, and evaluating $k_\perp^4$ by squaring the average $k_\perp^2$ defined in Ref. [4]. Representative curves are shown in Fig. (9).

The simple model predicts the region of high transport seen in nonlinear simulations reasonably well [Fig. (10)]. The high $\hat{s}$, low flux region has also been observed. Physically, high transport is predicted when the dominant modes shift to longer wavelengths. Local shear plays an important role in both the primary and the secondary. For $\gamma \sim \sqrt{\omega_d\omega_*\eta_e} - |k_\parallel|v_t$, instability requires $k_p\rho_e \gtrsim L_T/(qR)$, so that high q and high R/L_T produce large transport. Small L_n/R can be stabilizing.[18]

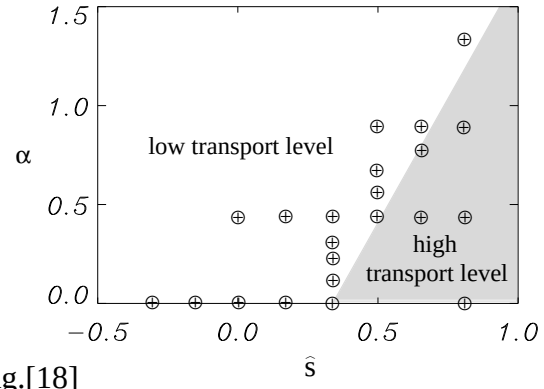

Figure 10: *Nonlinear simulation results for the reference parameters as a function of* $\hat{s}$ *and* α.

The nonlinear development of the secondary instabilities leads to the production of zonal flows, which are subject to tertiary instabilities. Ignoring the effects of background gradients, rotational symmetry in the perpendicular plane means that Eq. (7) also describes tertiary instabilities in ETG turbulence, so that secondary and tertiary modes in ETG turbulence are both weak. By contrast,

the electron response in ITG turbulence breaks this symmetry, so that while tertiary instabilities in the ITG system are weak, the secondary instabilities are strong. This is consistent with the larger role of zonal flows observed in ITG simulations, and larger normalized transport observed in ETG simulations.

In summary, we presented gyrokinetic simulations of electromagnetic ETG and electrostatic ITG turbulence. The transport from either is large enough to produce marginally stable temperature profiles for a wide range of experimental conditions. Simple models that balance primary instabilities against secondary instabilities, and zonal flows against tertiary instabilities, provide insight into the simulation results. ETG turbulence can drive transport as effectively as ITG turbulence and is naturally harder to stabilize with velocity shear, but may be controlled, *e.g.,* with local magnetic shear. At low q, ITG turbulence may be nonlinearly suppressed, but a collisionless tertiary instability limits the extent of the suppression.

References

[1] W. Dorland, PhD Thesis, Princeton, (1993); G. W. Hammett, *et al.*, PPCF, **35**, 973 (1993); M. A. Beer, PhD Thesis, Princeton, (1995); R. E. Waltz, *et al.*, Phys. Plas., **1**, 2229 (1994); A. M. Dimits *et al.*, PRL **77**, 71 (1996); Z. Lin *et al.*, Science **281**, 1835 (1998).

[2] A. M. Dimits *et al.*, Phys. Plasmas, **7**, 969 (2000).

[3] B. N. Rogers, W. Dorland, and M. Kotschenreuther, to appear, PRL (2000).

[4] M. Kotschenreuther, W. Dorland, G. W. Hammett, and M. A. Beer, Phys. Plasmas **2**, 2381 (1995); W. Dorland, *et al.*, 1994 IAEA Proceedings (Seville), **3**, 463 (1994).

[5] B. Coppi and G. Rewoldt, in *Advances in Plasma Physics*, edited by A. Simon and W. B. Thompson, volume 6, page 421, John Wiley and Sons, New York, 1976.

[6] B. Coppi, M. N. Rosenbluth and R. Z. Sagdeev, Phys. Fluids, **10**, 582 (1967).

[7] M. Zarnstorff, Bull. Am. Phys. Soc. **43**, 1635 (1999).

[8] B. W. Stallard, Phys. Plasmas **6**, 1978 (1999).

[9] S. C. Cowley, R. M. Kulsrud, and R. Sudan, Phys. Fluids B **3**, 2767 (1991).

[10] F. Jenko, W. Dorland, M. Kotschenreuther, and B. N. Rogers, Phys. Pl., **7**, 1904 (2000).

[11] W. Dorland, F. Jenko, M. Kotschenreuther, and B. N. Rogers, submitted to PRL (2000).

[12] M. A. Beer, S. C. Cowley, and G. W. Hammett, Phys. Plasmas **2**, 2687 (1995).

[13] W. Dorland and G. W. Hammett, Phys. Fluids B **5**, 812 (1993).

[14] M. N. Rosenbluth and F. Hinton, PRL **80**, 724 (1998).

[15] M. Greenwald, *et al.*, Nuclear Fusion **37**, 793 (1997).

[16] Z. Lin, *et al.*, PRL **83**, 3645 (1999).

[17] T. Antonsen and B. Lane, Phys. Fluids **23**, 1205 (1980); E. A. Frieman and L. Chen, Phys. Fluids **25**, 502 (1982).

[18] F. Romanelli and S. Briguglio, Phys. Fl. B , 754 (1990).